

Vertical integration of high- Q silicon nitride microresonators into silicon-on-insulator platform

Qing Li, Ali A. Eftekhar, Majid Sodagar, Zhixuan Xia,
Amir H. Atabaki, and Ali Adibi*

School of Electrical and Computer Engineering, Georgia Institute of Technology,
777 Atlantic Drive NW, Atlanta, GA 30332, USA.

*adibi@ece.gatech.edu

Abstract: We demonstrate a vertical integration of high- Q silicon nitride microresonators into the silicon-on-insulator platform for applications at the telecommunication wavelengths. Low-loss silicon nitride films with a thickness of 400 nm are successfully grown, enabling compact silicon nitride microresonators with ultra-high intrinsic Q s ($\sim 6 \times 10^6$ for 60 μm radius and $\sim 2 \times 10^7$ for 240 μm radius). The coupling between the silicon nitride microresonator and the underneath silicon waveguide is based on evanescent coupling with silicon dioxide as buffer. Selective coupling to a desired radial mode of the silicon nitride microresonator is also achievable using a pulley coupling scheme. In this work, a 60- μm -radius silicon nitride microresonator has been successfully integrated into the silicon-on-insulator platform, showing a single-mode operation with an intrinsic Q of 2×10^6 .

© 2013 Optical Society of America

OCIS codes: (130.3120) Integrated optics devices;(230.5750) Resonators.

References and links

1. G. T. Reed and A. P. Knights, *Silicon Photonics: An Introduction* (John Wiley, 2004).
2. A. W. Fang, H. Park, O. Cohen, R. Jones, M. J. Paniccia, and J. E. Bowers, “Electrically pumped hybrid AlGaInGs-silicon evanescent laser,” *Opt. Express* **14**, 9203–9210 (2006).
3. A. Liu, R. Jones, L. Liao, D. Samara-Rubio, D. Rubin, O. Cohen, R. Nicolaescu, and M. Paniccia, “A high-speed silicon optical modulator based on a metal-oxide-semiconductor capacitor,” *Nature (London)* **427**, 615–618 (2004).
4. Q. Xu, B. Schmidt, S. Pradhan, and M. Lipson, “Micrometer-scale silicon electro-optic modulator,” *Nature (London)* **435**, 325–327 (2005).
5. L. Chen and M. Lipson, “Ultra-low capacitance and high speed germanium photodetectors on silicon,” *Opt. Express* **17**, 7901–7906 (2009).
6. F. Xia, M. Rooks, L. Sekaric, and Y. Vlasov, “Ultra-compact high order ring resonator filters using submicron silicon photonic wires for on-chip optical interconnects,” *Opt. Express* **15**, 11934–11941 (2007).
7. F. Xia, L. Sekaric, and Y. Vlasov, “Ultracompact optical buffers on a silicon chip,” *Nature Photon.* **1**, 65–71 (2007).
8. M. Borselli, T. Johnson, and O. Painter, “Beyond the Rayleigh scattering limit in high- Q silicon microdisks: theory and experiment,” *Opt. Express* **13**, 1515–1530 (2005).
9. M. Soltani, S. Yegnanarayanan, and A. Adibi, “Ultra-high Q planar silicon microdisk resonators for chip-scale silicon photonics,” *Opt. Express* **15**, 4694–4704 (2007).
10. Q. Lin, O.J. Painter, and G.P. Agrawal, “Nonlinear optical phenomena in silicon waveguides: Modeling and applications,” *Opt. Express* **15**, 16604–16644 (2007).
11. J. F. Bauters, M. J. R. Heck, D. John, D. Dai, M. C. Tien, J. S. Barton, A. Leinse, R. G. Heideman, D. J. Blumenthal, and J.E. Bowers, “Ultra-low-loss high-aspect-ratio Si₃N₄ waveguides,” *Opt. Express* **19**, 3163–3174 (2011).

12. M. C. Tien, J. F. Bauters, M. M. R. Heck, D. J. Blumenthal, and J. E. Bowers, "Ultra-low loss Si₃N₄ waveguides with low nonlinearity and high power handling capability," *Opt. Express* **18**, 23562–23568 (2010).
13. G. Roelkens, D. Van Thourhout, R. Baets, R. Notzel, and M. Smit, "Laser emission and photodetection in an InP/InGaAsP layer integrated on and coupled to a Silicon-on-Insulator waveguide circuit," *Opt. Express* **14**, 8154–8159 (2006).
14. M. Ghulinyan, R. Guider, G. Pucker, and L. Pavesi, "Monolithic whispering-gallery mode resonators with vertically coupled integrated bus waveguide," *IEEE Photon. Technol. Lett.* **23**, 1166–1168 (2011).
15. F. Ramiro-Manzano, N. Prtljaga, L. Pavesi, G. Pucker, and M. Ghulinyan, "A fully integrated high-*Q* whispering-gallery wedge resonator," *Opt. Express* **20**, 22934–22942 (2012).
16. J. F. Bauters, M. L. Davenport, M. J. R. Heck, J. K. Doylend, A. Chen, A. W. Fang, and J. E. Bowers, "Silicon on ultra-low-loss waveguide photonic integration platform," *Opt. Express* **21**, 544–555 (2013).
17. T. Barwicz, M. A. Popovic, P. T. Rakich, M. R. Watts, H. A. Haus, E. P. Ippen, and H. I. Smith, "Microring-resonator-based add-drop filters in SiN: fabrication and analysis," *Opt. Express* **12**, 1437–1442 (2004).
18. E. S. Hosseini, S. Yegnanarayanan, A. H. Atabaki, M. Soltani, and A. Adibi, "High quality planar silicon nitride microdisk resonators for integrated photonics in the visible wavelength range," *Opt. Express* **17**, 14543–14551 (2009).
19. A. Gondarenko, J.S. Levy, and M. Lipson, "High confinement micron-scale silicon nitride high *Q* ring resonator," *Opt. Express* **17**, 11366–11370 (2009).
20. M. A. Foster, J. S. Levy, O. Kuzucu, K. Saha, M. Lipson, and A. L. Gaeta, "Silicon-based monolithic optical frequency comb source," *Opt. Express* **19**, 14233–14239 (2011).
21. J. F. Bauters, M. J. R. Heck, D. D. John, J. S. Barton, C. M. Bruinink, A. Leinse, R. G. Heideman, D. J. Blumenthal, and J. E. Bowers, "Planar waveguides with less than 0.1 dB/m propagation loss fabricated with wafer bonding," *Opt. Express* **19**, 24090–24101 (2011).
22. M. C. Tien, J. F. Bauters, M. J. R. Heck, D. T. Spencer, D. J. Blumenthal, and J. E. Bowers, "Ultra-high quality factor planar Si₃N₄ ring resonators on Si substrates," *Opt. Express* **19**, 13551–13556 (2011).
23. D. T. Spencer, Y. Tang, J. F. Bauters, M. J. R. Heck, and J. E. Bowers, "Integrated Si₃N₄/SiO₂ ultra high *Q* ring resonators," in *Photonics Conference* (Institute of Electrical and Electronics Engineers, Burlingame, CA, 2012), 141–142.
24. F. H. P. M. Habraken, *LPCVD Silicon Nitride and Oxynitride Films: Material and Applications in Integrated Circuit Technology* (Springer, 1991).
25. H. A. Haus, *Electromagnetic Fields and Energy* (Prentice Hall, 1989).
26. Q. Li, A. A. Eftekhar, Z. Xia, and A. Adibi, "Azimuthal-order variations of surface-roughness-induced mode splitting and scattering loss in high-*Q* microdisk resonators," *Opt. Lett.* **37**, 1586–1588 (2012).
27. Q. Li, A. A. Eftekhar, P. Alipour, A. H. Atabaki, S. Yegnanarayanan, and A. Adibi, "Low-loss microdisk-based delay lines for narrowband optical filters," *IEEE Photon. Technol. Lett.* **24**, 1276–1278 (2012).
28. E. S. Hosseini, S. Yegnanarayanan, A. H. Atabaki, M. Soltani, and A. Adibi, "Systematic design and fabrication of high-*Q* single-mode pulley-coupled planar silicon nitride microdisk resonators at visible wavelengths," *Opt. Express* **18**, 2127–2136 (2010).
29. Q. Li, M. Soltani, S. Yegnanarayanan, and A. Adibi, "Design and demonstration of compact, wide bandwidth coupled-resonator filters on a silicon-on-insulator platform," *Opt. Express* **17**, 2247–2254 (2009).
30. Z. Xia, A. A. Eftekhar, M. Soltani, B. Momeni, Q. Li, M. Chamanzar, S. Yegnanarayanan, and A. Adibi, "High resolution on-chip spectroscopy based on miniaturized microdonut resonators," *Opt. Express* **19**, 12356–12364 (2011).
31. C. W. Holzwarth, T. Barwicz, and H. I. Smith, "Optimization of hydrogen silsesquioxane for photonic applications," *J. Vac. Sci. Technol. B* **25**, 2658–2661 (2007).

1. Introduction

The silicon-on-insulator (SOI) platform has enabled impressive advances in many areas of integrated photonics [1]. For applications such as on-chip interconnects at the telecommunication wavelength range (i.e., 1300 – 1550 nm), key components, including hybrid silicon (Si) lasers [2], high-speed modulators and switches [3, 4], hybrid detectors [5], band-pass filters [6] and optical buffers [7] have all been demonstrated. Despite these impressive achievements, Si faces some major challenges arising from its inherent material properties. For example, Si cannot compete with silicon dioxide (SiO₂) or silicon nitride (SiN) for some passive devices such as low-loss delay lines in terms of insertion loss and power handling capability, for the following two reasons: (1) Si devices have a relatively large propagation loss (typically > 10 dB/m limited by scattering loss) due to their large refractive index contrast and small mode volume [8, 9]; (2) Si has strong nonlinear effects at high light intensities because of a large third-order

nonlinear coefficient and also the free carriers generated by the two-photon absorption process [10]. On the other hand, SiO₂ or SiN devices have one or two orders of magnitude smaller propagation loss (0.1 – 1 dB/m) [11] and one order of magnitude smaller nonlinear coefficient with no free carrier loss [12], resulting in much smaller nonlinear effects than Si devices under the same power level. Despite these advantages, active elements such as modulators and phase shifters are difficult to realize in SiO₂ or SiN due to the difficulty in tuning the refractive index of the host material, while Si devices can be easily tuned using the thermo-optic or the plasma-dispersion effect [1].

Therefore, a coherent integration of SiN and Si can naturally lead to more effective and functional devices, especially for applications requiring low-loss performance (e.g., delay lines) or high power handling (e.g., frequency comb sources). For this purpose, vertical integration can be used, which has been proven to be an efficient method to integrate materials with different properties [13, 14, 15]. In Ref. [16], a Si-on-SiN integrated platform has already been demonstrated for waveguides using a bonding process. In this work, we integrate high-*Q* SiN microresonators into the SOI platform by depositing SiN on top of SOI wafers. Such a SiN-on-SOI platform can preserve the quality of each material (especially for Si), and the fabrication process is also simpler compared to that in the bonding approach. Successful demonstration of low-loss coupled devices in this hybrid platform requires: 1) low-loss SiN films to enable high-*Q* SiN microresonators, and 2) optimal coupling between the SiN microresonators and Si waveguides in the SOI platform. In the rest of this paper, we focus on our approach in addressing these two requirements. Section 2 is focused on the demonstration of high-*Q* SiN microresonators on SiO₂, and Section 3 is devoted to the details of integration of the SiN layer to the SOI platform. Final conclusions are discussed in Section 4.

2. High-*Q* SiN microresonators on SiO₂

Within the areas of integrated photonics, SiN has been investigated for a range of applications. Initially, silicon-rich SiN is used as its low stress allows a thick SiN film (> 400 nm) without cracks [17]. Recently, the use of stoichiometric SiN (i.e., Si₃N₄) is also actively pursued [18]. Thick SiN films up to 700 nm have been grown, and compact microresonators with radii down to 20 μm and intrinsic *Q*s (i.e., unloaded *Q*s) around 3 million have been demonstrated [19, 20]. Another approach employs a thin layer of SiN (< 100 nm) as the guiding core, and ultra-low-loss waveguides (with propagation loss less than 0.1 dB/m) have been demonstrated [21]. High-*Q* microresonators are also reported based on the same platform (with intrinsic *Q*s up to 55 million for a 9.8-mm-radius microring), though the bending radii have to be in the order of millimeters to avoid significant radiation loss [22, 23].

For the purpose of dense integration, the SiN film has to be thick enough to enable compact microresonators and sharp waveguide bends. Numerical simulations show that a 400-nm-thick SiN layer permits the realization of microresonators with a radiation-limited *Q* more than a billion for radii as small as 40 μm. Low-pressure chemical vapor deposition (LPCVD) method is conventionally used for stoichiometric SiN deposition at temperatures around 800°C with standard source gases of dichlorosilane (SiH₂Cl₂, or DCS) and ammonia (NH₃). The gas ratio between dichlorosilane and ammonia is the dominant factor for both the film stress and the material absorption, and a tradeoff exists between these two material properties. For example, low-stress SiN films can be grown using a large dichlorosilane to ammonia ratio (e.g., 3 – 6) with thicknesses up to a few micrometers [24], but such films usually have a high hydrogen content, which is responsible for the strong N-H bond material absorption around the wavelength of 1.55 μm [24]. (N-H bond has a vibrational mode with wavelength around 3 μm and its second harmonic is around 1.55 μm.) Decreasing the dichlorosilane to ammonia ratio (e.g., 0.1 – 1) can reduce the hydrogen content, but the stress of the film increases significantly. Therefore,

for our applications, a careful balance between the film thickness and the material absorption has to be found. Also, an optimal post-annealing process has to be developed to further reduce the hydrogen content to minimize the material absorption loss.

As the first step of integrating SiN microresonators into the SOI platform, high- Q SiN microresonators are fabricated using SiN-on-SiO₂ wafers where the SiO₂ layer is thick enough ($> 3 \mu\text{m}$) to prevent leakage from the SiN layer to the Si substrate. The SiN deposition recipe is optimized using a Tystar Nitride LPCVD tool (DCS : NH₃ = 50 : 140 sccm at a pressure of 165 mT). To pattern the SiN samples, a JEOL JBX-9300FS electron-beam lithography (EBL) system is used with ZEP520A (by Zeon cooperation) as the e-beam resist, which is capable of defining fine features with a relatively good etch resistance. One problem with SiN is that it is an insulating material, and electrons can accumulate at the SiN surface as exposure progresses. This charge-up effect disturbs the EBL writing process, and under certain circumstances, it can become strong enough to cause fracture errors. To solve this problem, a conducting polymer, ESPACER (by Shawa Denko K.K.), is spin-coated on top of ZEP before the electron-beam exposure and is subsequently removed with deionized water before the development of ZEP. Next, the pattern is transferred to the SiN layer using plasma etching with a CF₄/CHF₃ gas mixture in an Oxford Endpoint reactive ion etching machine. The etching recipe is optimized based on SiN-on-Si samples, whose conducting Si substrate helps reduce the charge-up effect from SiN so good scanning-electron micrographs (SEMs) can be taken to examine the etching quality. Figure 1(a) shows the SEM of the cross section of a 400-nm-thick SiN waveguide structure, and fairly vertical and smooth sidewalls have been achieved. After etching, a 1- μm -thick SiO₂ is deposited on the SiN devices using the plasma-enhanced chemical vapor deposition process. Finally, the optimum annealing process is developed in a Tystar Poly Furnace, and the optimal recipe is found to be 8 hours in an O₂ ambient and 4 hours in a N₂ ambient at 1100°C [19].

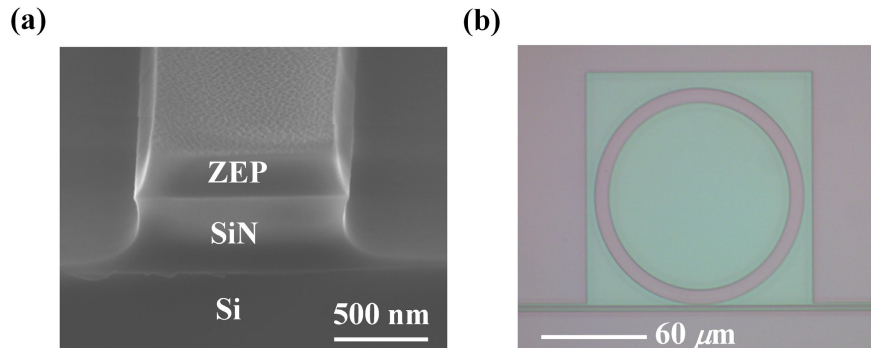


Fig. 1. (a) SEM of the cross section of a SiN waveguide structure with a width of 1.2 μm and a height of 400 nm. (b) Optical micrograph of a 60- μm -radius SiN microring with a width of 8 μm .

Using the developed fabrication recipe, SiN microresonators are fabricated on wafers with a 400-nm-thick SiN layer deposited on a thermally grown, 4- μm -thick oxide layer. Figure 1(b) shows the optical micrograph of a 60- μm -radius SiN microring with a width of 8 μm (the access waveguide has a width of 1.2 μm and the gap is 700 nm), whose transmission measurements for the TE-polarized light (i.e., electric field predominantly parallel to the device layer) before and after annealing are shown in Fig. 2(a). Figure 2(a) shows that before annealing,

the resonance dips for the wavelength range of 1490 – 1560 nm are much shallower than those outside this range, indicating a strong material absorption at these wavelengths. Such an absorption spectrum is characteristic of the overtone absorption from the N-H bond [24]. Figure 2(a) also shows that after applying the optimized annealing process, the resonance dips become more uniform across the whole wavelength range, indicating that the hydrogen content has been significantly reduced. Figure 2(b) shows the zoom-in figure for one specific resonance (marked in Fig. 2(a)) around the wavelength of 1530 nm. As can be seen, before annealing, the absorption-limited intrinsic Q is around 0.15 million, corresponding to a propagation loss around 235 dB/m; but after annealing, the intrinsic Q dramatically increases to 6 million, corresponding to a propagation loss around 6 dB/m.

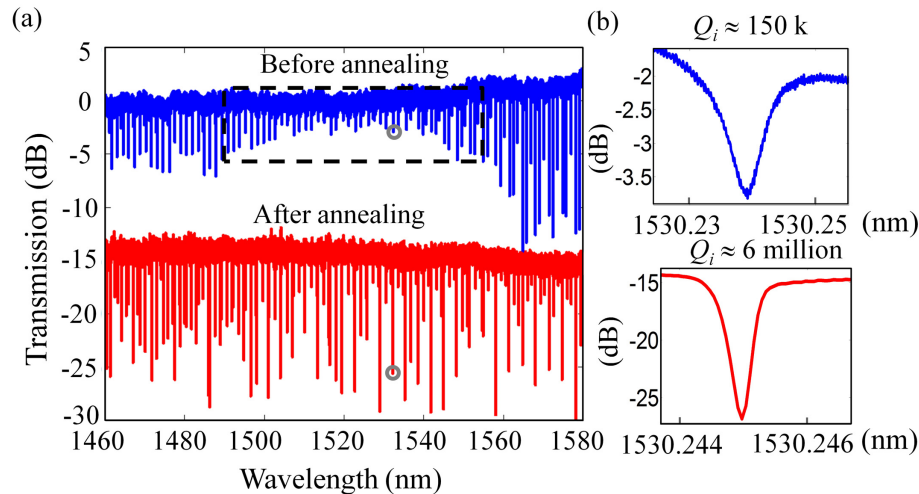


Fig. 2. (a) Transmission measurements for a 60- μm -radius microring resonator fabricated with a 400-nm-thick SiN layer on the SiO_2 substrate: the blue curve is before annealing and the red curve is after annealing (intentionally moved down by 15 dB for a better comparison). (b) Zoom-in figures for the resonance marked in (a): the upper figure is before annealing and the lower figure is after annealing.

In the next step, the limiting factor of the measured intrinsic Q is investigated. For our SiN microresonators whose radiation-limited Q is high enough (> 1 billion), there are two major sources of loss: 1) the material absorption loss from the remaining N-H bond after annealing, and 2) the scattering loss resulting from the sidewall roughness caused by fabrication imperfections. To distinguish these two loss effects, we can exploit their different scaling behaviors with the size of the resonator (i.e., R) [8]. To see that, we use Q 's definition as [25]

$$Q \equiv \frac{\omega \cdot U_c}{P_{\text{loss}}}, \quad (1)$$

where ω is the angular frequency; U_c is the energy of the resonant mode (that is proportional to the mode volume); and P_{loss} is the power dissipation rate. Since our microring width is large, the fundamental radial mode does not interact with the inner sidewall, and its mode volume scales with the radius R as R^2 , i.e., $U_c \propto R^2$ [8]. (The fundamental radial mode is essentially a microdisk mode whose radial expansion increases linearly with R . If the microring width is small, then the radial expansion is limited by the ring width as a constant and its mode volume only scales linearly with R .) The material absorption loss is a volume effect that is proportional to the mode volume, i.e., $P_{\text{loss,abs}} \propto R^2$. Therefore, if the resonator is limited by the material

absorption loss, its intrinsic Q will not depend much on R . On the other hand, the sidewall scattering loss is a surface effect, indicating it scales linearly with R (assuming the field intensity at the periphery stays the same while scaling), i.e., $P_{\text{loss, scat}} \propto R$. As a result, if the resonator is limited by the sidewall scattering loss, the intrinsic Q will almost linearly increase with R . (Rigorous numerical simulation gives slightly lower estimate. For example, the scattering Q at $R = 240 \mu\text{m}$ is 5.54 of that at $R = 40 \mu\text{m}$.) In Fig. 3, the intrinsic Q s of the fundamental radial mode for several independently fabricated microresonators with radii ranging from $20 \mu\text{m}$ to $240 \mu\text{m}$ are shown, where each circle represents one measurement result and the dotted black line is the statistical average. From the almost linear behavior of the average intrinsic Q with R , we conclude that the intrinsic Q of our SiN microresonators is mainly limited by the sidewall scattering loss and not the material absorption loss.

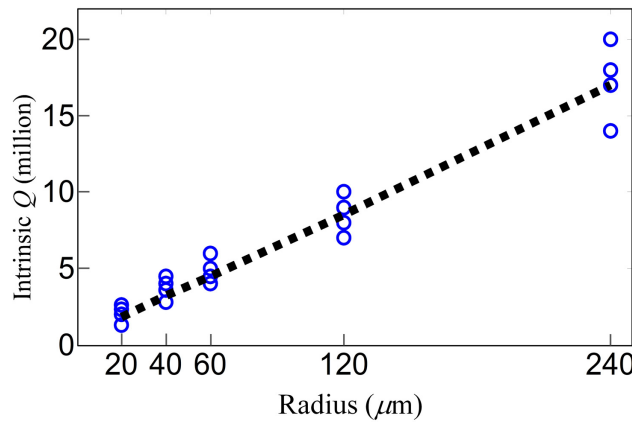


Fig. 3. Measured (circles) intrinsic Q s of the fundamental radial mode from independently fabricated SiN microrings with different radii (the width of the microrings is kept the same as $8 \mu\text{m}$). The dotted black line is the statistical average.

In Fig. 4, the transmission spectrum of a $240\text{-}\mu\text{m}$ -radius microring (with a width of $8 \mu\text{m}$) is plotted, and different radial mode families are identified by comparing the measured free spectral ranges (FSRs) with the simulation results (see Appendix A for details). The insets to Fig. 4 depict the lineshapes of several resonances belonging to the first- and second-order radial modes, whose intrinsic Q s are measured to be between $17 - 20$ million (propagation loss $\sim 2 \text{ dB/m}$). We also observe that the mode splittings of these resonances are varying. For example, for the second-order radial mode, the mode splitting for the resonance around 1567.4 nm is negligible while it is strong for the one around 1568.2 nm . Such variations of mode splitting and intrinsic Q are characteristic of a scattering-loss limited microresonator [26]. In addition, for a microdisk resonator, higher-order radial modes usually have larger FSRs (or smaller group indices) and weaker scattering losses. For the $240\text{-}\mu\text{m}$ -radius microring, however, this is not the case. Starting from the third-order radial mode, the interaction between the resonant mode and the inner sidewall becomes important and increases with the radial mode order. Consequently, these radial modes tend to exhibit smaller FSRs (or larger group indices) and stronger scattering losses (and thus lower intrinsic Q s).

3. Integrating SiN microresonators into the SOI platform

The second step of this work is to integrate high- Q SiN microresonators into the SOI platform. As illustrated by Fig. 5, we have adopted a vertical integration approach by depositing SiN films

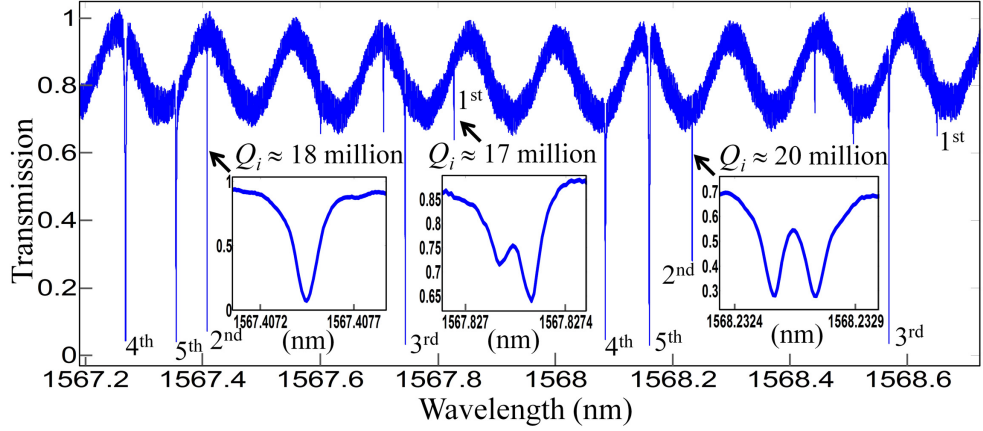


Fig. 4. Transmission spectrum of a 240- μm -radius SiN microring on SiO_2 with a width of 8 μm and SiN thickness of 400 nm. Different radial mode families are labeled by their radial mode orders, and the insets depict the lineshapes of the marked resonances.

on top of the SOI wafers with SiO_2 as buffer. The coupling between the SiN microresonator and the underneath Si waveguide is based on evanescent field overlap and in principle could be lossless [25]. Moreover, the SiO_2 thickness can be varied to adjust the coupling strength between the SiN and Si devices. In Section 2, we showed that high intrinsic Q s can be obtained for the first few radial modes of a wide microring, while higher-order radial modes with lower intrinsic Q s and different wavelength dispersions coexist. For applications such as low-loss delay lines based on over-coupled microresonators [27], a strong coupling to one of the high- Q radial modes is needed while the coupling to the other radial modes has to be suppressed. On the other hand, for applications such as wavelength conversion based on the four-wave mixing process [20], achieving a critical coupling to one of the high- Q radial modes for the pump is preferred (to get strong field enhancement). It is also possible to employ the high-order radial modes with relatively low Q s for the signal and idler (to allow large bandwidth) by engineering the inner sidewall to satisfy the energy and momentum conservation [20]. Therefore, to device designers, it is important to have the capability to achieve a selective and controllable coupling to a specific radial mode. For this purpose, we use the pulley coupling scheme in a vertical coupling architecture in the SiN-on-SOI hybrid platform [27, 28].

3.1. Vertical coupling based on the pulley coupling scheme

The pulley-coupled structure is illustrated by Fig. 6(a), which consists of a Si waveguide wrapped around the SiN microresonator for a certain coupling length. Using the first-order coupled-mode theory, the amplitude coupling coefficient between the n th ($n = 1, 2, \dots$) radial-order resonant mode (SiN) and the mode of the access waveguide (Si) is given by [25]

$$t_{n,m} = \frac{i\omega\epsilon_0}{4} \iiint_{\delta V_{\text{WG}}} (n_{\text{Si}}^2 - n_{\text{SiO}_2}^2) \mathbf{E}_{n,m}^*(\mathbf{r}) \cdot \mathbf{E}_{\text{WG}}(\mathbf{r}) d^3 r, \quad (2)$$

where $i = \sqrt{-1}$; ϵ_0 is the vacuum permittivity; δV_{WG} denotes the volume of the access waveguide (Si); n_{Si} and n_{SiO_2} are the refractive indices of Si and SiO_2 (cladding), respectively; $\mathbf{E}_{n,m}(\mathbf{r})$ is the electric field of the n th radial mode (of the SiN microresonator) with an azimuthal order m (the field is normalized so it corresponds to unit energy, i.e., $1/2 \int \epsilon(\mathbf{r}) |\mathbf{E}_{n,m}(\mathbf{r})|^2 dV = 1$ with $\epsilon(\mathbf{r})$ being the permittivity of an isolated microresonator); and $\mathbf{E}_{\text{WG}}(\mathbf{r})$ is the electric field

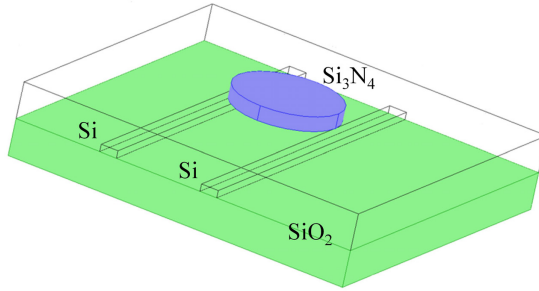


Fig. 5. Illustration of the vertical integration of SiN into the SOI platform: SiO₂ is the buffer between these two layers.

of the Si access waveguide (the field is normalized so it corresponds to unit power, i.e., $1/2 \int \text{Re}(\mathbf{E}_{\text{WG}}(\mathbf{r}) \times \mathbf{H}_{\text{WG}}^*(\mathbf{r}) \cdot \hat{\mathbf{k}}) dS = 1$, where $\mathbf{H}_{\text{WG}}(\mathbf{r})$ is the magnetic field, $\hat{\mathbf{k}}$ is the wave propagating direction and S is the transverse area of the waveguide).

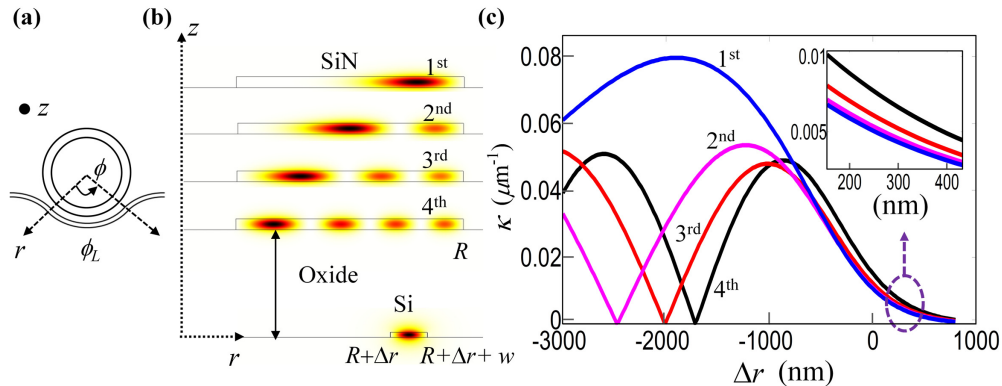


Fig. 6. (a) Schematic of the pulley coupling scheme. In the actual structure, the access waveguide is in the Si layer which is vertically separated from the SiN resonator by an oxide layer. (b) The radial cross section (r - z plane) of the SiN-Si vertically coupled structure. The mode profiles of the first four radial modes of a 240- μm -radius SiN microresonator (width 8 μm) and the Si waveguide are provided. (c) Computed κ as a function of the Si waveguide position for a fixed SiO₂ thickness of 500 nm for the first four radial-order modes of the SiN resonator. The inset shows a zoom-in view of κ for Δr in the range of 200 – 400 nm.

Equation (2) can be simplified for the pulley structure by considering the azimuth direction (i.e., ϕ as shown in Fig. 6(a)) and the transverse plane (i.e., r and z as shown in Fig. 6(a)) separately. As illustrated in Fig. 6(b), we use $R + \Delta r$ to denote the position of the inner sidewall of the Si waveguide, where R is the radius of the SiN microresonator and w is the width of the Si waveguide. Using the relations $\mathbf{E}_{n,m}(\mathbf{r}) = \mathbf{E}_n(r,z) \exp(im\phi)$ and $\mathbf{E}_{\text{WG}}(\mathbf{r}) = \mathbf{E}_{\text{WG}}(r,z) \exp[i\beta_{\text{WG}}(R + \Delta r + w/2)\phi]$ with β_{WG} being the propagation constant of the waveguide mode, we arrive at

$$t_{n,m} = i\kappa_n L \operatorname{sinc}\left(\frac{\delta\beta_{n,m}L}{2}\right), \quad (3)$$

where κ_n is defined as

$$\kappa_n \equiv \frac{\omega\epsilon_0}{4} \iint_{\delta S_{WG}} (n_{Si}^2 - n_{SiO_2}^2) \mathbf{E}_n^*(r, z) \cdot \mathbf{E}_{WG}(r, z) dr dz, \quad (4)$$

with δS_{WG} being the cross section of the Si waveguide; L is the coupling length ($L = \phi_L(R + \Delta r + w/2)$ with ϕ_L being the pulley coupling angle as shown in Fig. 6(a)); $\text{sinc}(x) \equiv \sin(x)/x$; and $\delta\beta_{n,m} \equiv m/(R + \Delta r + w/2) - \beta_{WG}$. (The dependence of $\delta\beta_{n,m}$ on the radial mode n is implicit, in the sense that around a given wavelength, different radial modes have different m , or, different effective indices.)

According to Eq. (3), if we adjust the access waveguide dimension (and thus, β_{WG}) to make the desired radial mode phase matched ($\delta\beta_{\text{desired},m} \approx 0$) and other radial modes phase mismatched, a proper choice of L can result in a suppressed coupling to the undesired radial modes [27]. However, for a large resonator, the difference between the effective indices of different radial modes is small, and the required coupling length can be very large (L should be on the order of $2\pi/|\delta\beta_{\text{undesired},m}|$). In our case, the vertical coupling allows us to place the Si waveguide underneath the SiN microresonator, which offers us an additional degree of freedom to differentiate κ_n in Eq. (3) among different radial modes. In Fig. 6(b), the mode profiles of the first four radial modes of a $240\text{-}\mu\text{m}$ -radius SiN microring (width $8\text{ }\mu\text{m}$) are plotted, and one can intuitively expect that when the Si waveguide is underneath the mode center of the n th radial mode, κ_n will reach its maximum. Using Eq. (4), κ_n for the first four radial modes (i.e., $n = 1 - 4$) as a function of the Si waveguide position are numerically calculated, and the results are provided in Fig. 6(c). The Si waveguide dimensions are chosen to be $400\text{ nm} \times 100\text{ nm}$ so its fundamental TE mode is almost phase-matched to the SiN resonant modes ($n_{eff} \approx 1.6$). The oxide thickness is fixed as 500 nm . As observed from Fig. 6(c), for $\Delta r \approx -2000\text{ nm}$, κ_1 is at least three times of other κ_n ($n \neq 1$), implying that even without phase-matching engineering, the power coupling coefficient ($|t_{n,m}|^2$) between the access waveguide and the fundamental radial mode is almost one order of magnitude stronger than that for a different radial mode. On the other hand, when $\Delta r > 0$, κ_n increases with the radial order n (see the inset of Fig. 6(c)), similar to laterally coupled structures. In such cases, the fundamental mode is difficult to excite using the conventional point coupling scheme, since κ_1 is much smaller than others [9].

3.2. Experimental demonstration

The fabrication process to integrate the SiN microresonator into the SOI platform are explained in the following: (a) starting with an SOI wafer with a Si thickness in the range of $80 - 110\text{ nm}$ and a $3\text{-}\mu\text{m}$ -thick buried oxide layer, the Si device layer is first patterned using hydrogen silsesquioxane (HSQ, also called XR-1541, which is a negative resist with similar chemical properties as SiO_2) as the EBL resist and then dry etched using a Cl_2 -based plasma [29, 30]; (b) flowable oxide (FOx(R)-16 by Dow Corning) is spin-coated on top of SOI, resulting in an almost flat surface (see the SEM shown in Fig. 7(a)) with film thickness around $550 - 750\text{ nm}$ (depending on the spin-coat speed). The FOx film is first cured at 350°C on a hotplate for 1 hour and then annealed in the oxygen ambient at 800°C to convert it to SiO_2 (Si-H bond removed) [31], as can be confirmed from the SEM shown in Fig. 7(b); (c) using the LPCVD method, a 400-nm -thick SiN is deposited on top of the SiO_2 buffer (see Fig. 7(b)), and annealing is performed to remove the N-H bond; (d) in order to align the SiN microresonators to the underneath Si waveguides, we have markers made in the Si layer. However, because of the strong charge-up effect from the top SiN and SiO_2 layers, the Si markers are difficult to find under the SEM of the EBL system. To solve this problem, photolithography is employed to open a window ($2\text{ mm} \times 2\text{ mm}$) on top of the Si markers, which can be exposed by removing the top SiN and SiO_2 layers using a dry etching process (CF_4); (e) SiN microresonators are

fabricated after alignment to the underneath Si waveguides using the Si markers. The optical micrograph in Fig. 7(c) demonstrates that a good alignment between the SiN microresonator and the underneath Si waveguide has been achieved.

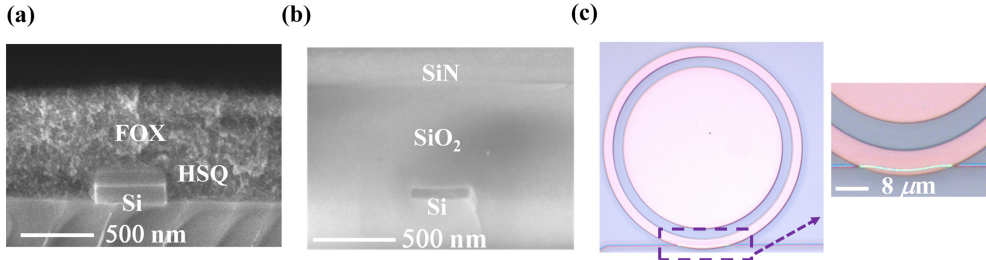


Fig. 7. (a) SEM showing the cross section of the Si waveguide ($400 \text{ nm} \times 100 \text{ nm}$) after the coating of FOx ($\sim 550 \text{ nm}$). The remaining HSQ is about 70 nm after Si etching. (2) SEM showing the cross section of the Si waveguide ($400 \text{ nm} \times 80 \text{ nm}$) after the FOx ($\sim 750 \text{ nm}$) annealing and the SiN deposition. (c) Optical micrograph of a $60\text{-}\mu\text{m}$ -radius SiN microresonator coupled to an underneath Si waveguide. The right figure shows a zoom-in view of the coupling region.

As illustrated by Fig. 8(a), the fabricated samples are characterized by coupling light from a tunable laser to the Si waveguide input and collecting the transmitted light at the Si waveguide output. When the swept wavelength of the laser coincides with the resonances of the SiN microresonator, strong scattering light can be observed from the top infrared camera (see Fig. 8(a)), indicating a good coupling between the Si and SiN layers. The transmission spectrum for a $60\text{-}\mu\text{m}$ -radius SiN microring is provided in Fig. 8(b), where only the fundamental radial mode is excited due to the use of the pulley coupling scheme (Si waveguide: $450 \text{ nm} \times 110 \text{ nm}$ (intentionally designed to be phase mismatched to the first-order radial mode with $\delta\beta_1 \sim -0.4 \text{ rad}/\mu\text{m}$ so a critical coupling can be achieved), $\Delta r \approx -2000 \text{ nm}$, $L \approx 10 \text{ }\mu\text{m}$, and oxide thickness $\approx 700 \text{ nm}$). The zoom-in figure for the marked resonance in Fig. 8(b) is also provided, suggesting an intrinsic Q of 2 million. Note that this Q value is about 40% of what we can get from a SiN-on-SiO₂ structure. (The statistical average of intrinsic Q s for $60\text{-}\mu\text{m}$ -radius microresonators is around 4.5 million, see Fig. 3.) The reduction of the intrinsic Q has also been confirmed by fabricating SiN microresonators on the oxide substrate along with the SiN-on-SOI samples. Processed by identical fabrication steps, the intrinsic Q s of SiN-on-SOI samples are consistently lower (about half) than those obtained for SiN-on-SiO₂ ones. We believe the reduction of the intrinsic Q s is mainly due to the degradation of the SiN material quality deposited on the FOx surface, which is not perfectly flat as can be seen from Fig. 7(a). In the future, a chemical-mechanical polishing (CMP) for the FOx layer should improve the SiN quality and therefore the intrinsic Q s of SiN microresonators. Nevertheless, the results shown in Fig. 8 demonstrate the potential of forming low-loss devices in the SiN-on-SOI platform with considerably better performance measures (e.g., loss, maximum allowed intensity, tuning and reconfiguration features) compared to either the conventional SOI-based structures or the SiN-on-SiO₂ structures.

4. Conclusion

In summary, we demonstrated here a vertical integration of high- Q SiN microresonators into the SOI platform for applications requiring low-loss performance or a high power handling capability at the telecommunication wavelength range. Using a 400-nm-thick SiN layer, com-

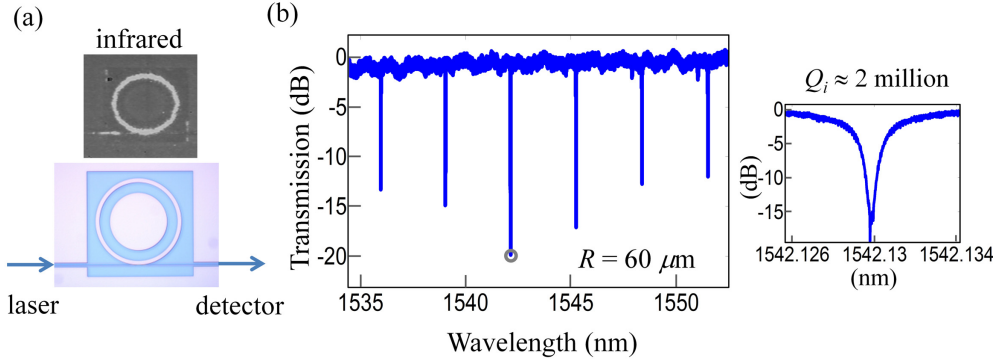


Fig. 8. (a) Illustration of the characterization process for the SiN-on-SOI samples: light is coupled from a tunable laser into the Si waveguide input and then collected at the Si waveguide output before sent to the detector. The top image is captured by an infrared camera when the SiN microresonator is at resonance. (b) Transmission spectrum measurement for a 60- μm -radius SiN microring fabricated on top of SOI, showing an intrinsic Q around 2 million. The optical micrograph of the coupled structure is shown in Fig. 7(c): the Si waveguide's dimensions are 450 nm \times 110 nm, $\Delta r \approx -2000$ nm, $L \approx 10 \mu\text{m}$, and oxide thickness ≈ 700 nm.

pact SiN microresonators have been successfully fabricated; especially, the ultra-high Q of 20 million (propagation loss around 2 dB/m) for a 240- μm -radius microring is, to the best of our knowledge, the largest reported to date for SiN microresonators at such size levels. The integration of SiN microresonators with SOI has been achieved by depositing SiN on top of the SOI devices using SiO₂ as the buffer. We showed the possibility of achieving selective coupling to one of the radial modes (in particular, the high- Q fundamental radial mode) of a wide SiN microring based on the vertical pulley coupling scheme. Microrings with a 60- μm -radius have been demonstrated on such a SiN-on-SOI platform, showing a single-mode operation with an intrinsic Q around 2 million. The decrease of the intrinsic Q compared to those obtained from the SiN-on-SiO₂ samples is believed to arise from the degradation of the SiN material quality deposited on the uneven SiO₂ buffer, whose surface quality could be improved by a CMP process in future to allow for higher intrinsic Q s of SiN microresonators integrated into the SOI platform.

Appendix A: Characterization details

The tunable laser used in the transmission measurement is Agilent 81682A with a tunable wavelength range of 1460 – 1580 nm and a linewidth of 100 kHz. The laser is set at a high output power ($> 500 \mu\text{W}$) to minimize the noise from the spontaneous emission. (For example, if the laser is set at 50 μW , a resonance with a large extinction ratio (> 15 dB) could be measured to be less than 10 dB due to the incoherent background noise from the laser, even the signal received by the detector is strong enough.) The light is attenuated externally to avoid nonlinear effects in the high- Q microresonator. To measure high- Q resonances, wavelengths are continuously scanned (continuous mode) at the slowest scan speed (500 pm/s), and the signal collected by the detector (Thorlabs PDB150C 800 – 1700 nm) is sampled at 40k – 80k sample/s by the data acquisition (DAQ) board (National Instruments PCI 6259). The scan linearity of the laser under such settings has been verified to be good (see discussions below), and the transmission results provided in the paper are plotted as measured (except that the baseline of the intensity has been shifted).

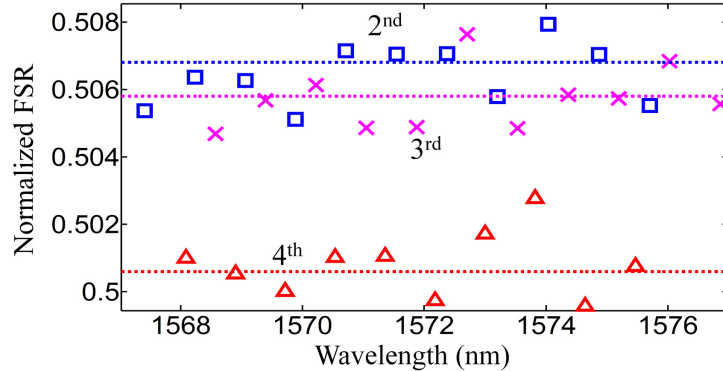


Fig. 9. Measured and normalized FSRs for three different radial modes from the transmission spectrum plotted in Fig. 4: 2nd (square), 3rd (cross) and 4th (triangle). The dotted lines are the corresponding simulation results.

In the measured transmission spectrum, we can start with an arbitrary resonance and find its radial mode family using an approximate FSR (~ 800 pm for 240 μm radius). The FSRs for the picked radial mode family can then be accurately measured from the transmission spectrum. Three such examples for the transmission plotted in Fig. 4 are provided in Fig. 9, where the normalized FSR is defined as $\text{FSR} \times 2\pi R/c = 1/n_g$, with n_g being the group index. The three dotted lines in Fig. 9 are the simulation results. For the 240- μm -radius microring with a width of 8 μm , the second-order radial mode has the largest FSR, and starting from the third-order radial mode, the FSRs decrease with the radial mode order due to the impact from the inner sidewall. Comparing the measured FSRs to the simulation results, the radial mode order of each resonance family can be identified. Figure 9 also shows that the scan of the laser is not strictly linear, since the measured FSRs are oscillating around its theoretical value with a relative error around $\pm 0.25\%$, indicating that there is about ± 2 pm error in the resonance wavelength measurement. (For small microresonators, the mode splitting could also contribute some errors in determining the exact resonance wavelength. But here, the mode splitting is on the order of 0.3 pm and could be neglected.)

The next question is how accurate the measured intrinsic Q s are since the slowest scan rate (500 pm/s) of the continuous mode is still fast. The tunable laser (Agilent 81682A) offers a wavelength locking mode that allows a narrowband scan around a desired wavelength (starting wavelength) by applying a sweeping low-frequency voltage (-5 V to 5 V). Figure 10(a) shows the transmission measurement using the continuous mode for another 240- μm -radius microring around the wavelength of 1568.6 nm (second-order radial mode), which shows a measured intrinsic Q around 16.7 million. Figure 10(b) shows the narrowband scan using the wavelength locking mode for the same resonance by applying a triangular wave (-5 V to 5 V, 1 kHz frequency, sampled at 100k sample/s; starting wavelength 1568.5 nm), where the forward and backward scans do not overlap due to the hysteresis associated with the piezo tuning. To correct the hysteresis and also to obtain an accurate wavelength range, the same wavelength scan is applied to measure the transmission spectrum of a long waveguide (~ 10 cm), which is a regular Fabry-Perot (FP) pattern with a period ~ 10 pm and could be used as reference. (The FP results from reflections at the cleaved facets. The same-type pattern can be observed in Fig. 4 with a larger period.) After such a calibration, the intrinsic Q is measured to be around 16 million. Therefore, we conclude that the transmission results from the continuous scan are accurate.

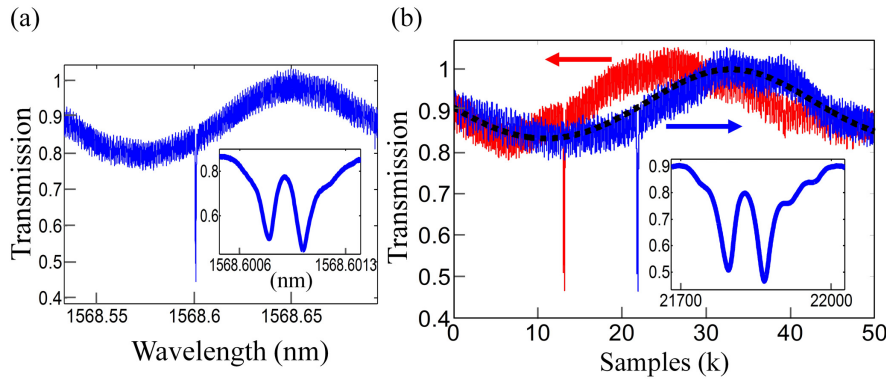


Fig. 10. (a) Transmission spectrum measured for a 240- μm -radius SiN-on-SiO₂ microresonator using the continuous mode of the tunable laser (500 pm/s, 80k sample/s sampling rate). The inset shows the lineshape of a resonance around 1568.6 nm. (b) Transmission spectrum measured for the same resonance shown in (a) using the wavelength locking mode of the tunable laser. The applied voltage to the laser is a triangle wave with a frequency of 1 kHz. It is generated by the DAQ board and sampled at 100k sample/s. The blue and red curves depict the forward and backward scans, respectively; and the dotted black line is the ideal FP response assuming a linear scan; and the inset shows the lineshape of the resonance around 1568.6 nm from the forward scan.

Acknowledgement

The authors would like to thank Devin Brown for help in solving the charge-up problem during the EBL process. This work was supported by the Air Force Office of Scientific Research under Grant No. FA9550-13-1-0032 (G. Pomrenke).